Numerical simulations of flows in cerebral aneurysms using the lattice Boltzmann method with single- and multiple-relaxation time collision models

Osaki, Susumu ; Hayashi, Kosuke ; Kimura, Hidehito ; Seta, Takeshi ; Kohmura, Eiji ; Tomiyama, Akio

(Citation)
Computers & Mathematics with Applications,78(8):2746-2760

(Issue Date)
2019-10-15

(Resource Type)
journal article

(Version)
Accepted Manuscript

(URL)
https://hdl.handle.net/20.500.14094/90006466

Numerical Simulations of Flows in Cerebral Aneurysms Using the Lattice Boltzmann Method with Single- and Multiple-Relaxation Time Collision Models

Susumu Osaki[a], Kosuke Hayashi[a,*], Hidehito Kimura[b], Takeshi Seta[c], Eiji Kohmura[b], Akio Tomiyama[a]

[a] *Graduate School of Engineering, Kobe University, 1-1 Rokkodai Nada Kobe Hyogo, 657-8501 Japan*
[b] *Graduate School of Medicine, Kobe University, 7-5-1, Kusunoki Chuo Kobe Hyogo, 650-0017 Japan*
[c] *Graduate School of Science and Engineering for Research, University of Toyama, 3190 Gofuku Toyama, 930-8555 Japan*

Abstract

Lattice Boltzmann simulations of flows in TOF-MRA-based cerebral aneurysm models are carried out using the single-, two- and multiple-relaxation time collision models, SRT, TRT and MRT, to investigate the effects of the collision model on predicted velocity fields in the aneurysms. The non-Newtonian characteristics of blood is accounted for by using the Casson model, whereas a simulation with the Newtonian viscous stress model is also carried out to investigate the effects of the viscous stress model on predicted velocity and wall shear stress distributions. Four cerebral aneurysm models are used in the simulation. The shapes of cerebral arteries are extracted from TOF-MRA data as STL meshes, and the level set function representing the artery wall is reconstructed from the STL mesh data. By making use of the level set function in the interpolated bounce-back scheme, the complex structures of arteries having aneurysms can be easily dealt with in the LB framework. As a result, the following conclusions are obtained: (1) the SRT can give reasonable predictions comparable to the MRT, provided that the spatial resolution is high enough; otherwise numerical errors can be large and numerical instabilities take place, (2) numerical errors in velocity is apt to take place in the near aneurysm wall region due to a small velocity scale, (3) although the TRT is less stable than the MRT, predictions of the TRT under stable numerical conditions are almost the same as those of the MRT, and (4) although the Bingham number effect on the flow structure is small, the mean wall shear stress may change over several percent, depending on the configuration of the aneurysm and the main blood flow, by neglecting the non-Newtonian nature of blood.

Keywords: multiple-relaxation time collision model, two-relaxation time collision model, TOF-MRA, Casson fluid, wall shear stress

*Corresponding author
Email address: hayashi@mech.kobe-u.ac.jp (Kosuke Hayashi)

1. Introduction

A cerebral aneurysm is a saccular dilatation forming on cerebral arteries. Rupture of a cerebral aneurysm causes swift death or poor prognosis at a high probability. Most cerebral aneurysms, therefore, are either stented or clipped to prevent rupture when they are found in CTA (computed tomography angiography) or MRA (magnetic resonance angiography). If cerebral aneurysms are known to hardly rupture under the patient specific condition, such surgery burdensome for patients can be avoided. We, however, do not have criteria for judging whether an aneurysm grows or not. Understanding the mechanism of the aneurysm growth is therefore of great demand of neurosurgeons and CFD-aided hemodynamics has been attracting much attention from the medical and engineering fields.

Naiver-Stokes (NS) equation-based simulations of blood flows have been carried out so far. Lou and Yang (1993) used the Casson model (Casson, 1959) to simulate the non-Newtonian nature of blood and predicted a blood flow about a channel bifurcation. Neofytou and Drikakis (2003) compared the characteristics of three non-Newtonian fluid models in flows with a sudden expansion. These studies focused on the non-Newtonian characteristics of blood and the channel geometries were much simpler than real blood vessels. Numerical simulations using real blood vessel models have been carried out by making use of three-dimensional (3D) models obtained in angiography. Cebral et al. (2005) modeled aneurysms from 3DRA (three-dimensional rotation angiography) and carried out NS-based simulations of non-Newtonian fluid flows in the models. They pointed out that the geometry of the vascular structure has a greater impact on predicted flow fields compared to the other parameters, e.g. the mean flow rate and the spatial resolution. Oshima et al. (2005) investigated the effects of a secondary flow caused at a curved section of an artery on the fluid motion and modeled an inflow velocity condition for an image-based cerebrovascular flow simulation by taking into account the secondary flow effect. They (Torii et al., 2006) extended their finite-element solver so as to deal with the fluid-structure interaction between the blood flow and the vessel motion. Kimura et al. (2019b) used the commercial software, hemoscope, and CTA-based cerebral aneurysm models to investigate a relation between the thickness of an aneurysm wall and a hemodynamic factor.

Most of the real aneurysm models used in the above numerical simulations were reconstructed from CTA images since CTA can give relatively high contrasted vessel images compared with TOF-MRA (time-of-flight magnetic resonance angiography). CTA is however invasive and is a burden to patients due to the use of a contrast medium, and therefore, it is not frequently acquired for a patient having a cerebral aneurysm. This makes it difficult to know the previous state of a cerebral aneurysm before its growth/rupture, in other words the key factors in the aneurysm growth. On the other hand, owing to the non-invasive nature, TOF-MRA data are acquired more frequently, and we can classify aneurysms into either a growing group or a non-growing group by observing the progress of the aneurysm size. We (Kimura et al., 2019a) therefore proposed to use TOF-MRA data in the CFD-aided hemodynamics to carry out a number of patient-specific simulations of flows in aneurysms. The lattice Boltzmann method (LBM) (Chen and Doolen, 1998) could be a reasonable choice for simulating flows in cerebral aneurysm models reconstructed from TOF-MRA data for many

cases since complex boundary shapes can be easily dealt with in the LBM.

Several LB simulations using real aneurysm models have been carried out in the last decade. Bernsdorf and Wang (2009) and Weichert et al. (2013) used the LBM to simulate a flow in a cerebral aneurysm modeled from medical images. The no-slip boundary condition at the aneurysm wall was accounted for by using the standard bounce-back scheme (Chen and Doolen, 1998), which is not accurate for curved boundaries. He et al. (2009) reconstructed a level set function, ψ, (Sussman et al., 1994) from voxel-based 3DRA data using the fast marching method (Sethian, 2001) to represent the vessel wall and it was used in the interpolated bounce-back scheme (Pan et al., 2006), whose accuracy for curved boundaries is better than that of the standard bounce-back scheme. These LB simulations for real aneurysms used the single-relaxation time (SRT) collision model (Qian et al., 1992). In general, this collision model is apt to cause numerical errors in the velocity distribution (Seta et al., 2014). It is important to make numerical errors in the velocity close to the aneurysm wall small to accurately evaluate the wall shear stress, which has been considered as one of the most important hemodynamic factors related with the aneurysm growth. Implementing the multiple-relaxation time (MRT) collision model is expected to predict the fluid flow close to the wall more accurately than the SRT. However the effects of the collision model on predicted velocity fields in cerebral aneurysms have not been discussed yet.

Non-Newtonian viscous stress models have been implemented in the LBM (Gabbanelli et al., 2005; Ashrafizaadeh and Bakhshaei, 2009; Boyd et al., 2009; Ohta et al., 2011). Ohta et al. (2011) carried out numerical simulations of two-dimensional flows in complex channel geometries using a modified Bingham model and the Casson model. The models successfully predicted the non-Newtonian behavior of the fluids, i.e. the formation of a plug core region in a channel between parallel flat plates. Applications of the non-Newtonian models are rarely found in literature concerned with CFD of aneurysms (Cebral et al., 2005; Bernsdorf and Wang, 2009; Kim et al., 2010; Huang et al., 2013) since the non-Newtonian effect has been considered to be weak in cerebral arteries due to a low shear rate (He et al., 2009). Cebral et al. (2005) carried out NS-based simulations of blood flows in four cerebral aneurysms and investigated the effects of the viscous stress model on the blood flow characteristics using the Newtonian and Casson models. They qualitatively compared velocity distributions in the cerebral aneurysms predicted with these models and confirmed that the flow characteristics are not affected by the viscous stress model except for a low flow rate case. Bernsdorf and Wang (2009) used the LBM, in which the Carreau-Yasuda non-Newtonian viscous stress model (Carreau, 1972) was implemented, to simulate a blood flow in a cerebral artery with an aneurysm. They pointed out that the shear thinning effect decreases the peak value of a wall shear stress in the aneurysm neck region. Only the single aneurysm model was however used in their study, and they focused on the effects of the viscous stress model on the wall shear stress in the aneurysm neck region and did not discuss the wall shear stress in the sac region. Huang et al. (2013) carried out LB simulations of flows in stented aneurysm models and reported some effects of the non-Newtonian model on the flows in the aneurysms, e.g. the Newtonian viscous stress model is apt to give a higher wall shear stress in an aneurysm neck region, whereas the effect of the viscous stress model is very small when an aneurysm is stented. They however used artificial aneurysm models

(straight channels with single circular cavities), which are much simpler than real cerebral aneurysms. In spite of the several findings obtained in the literature, our knowledge on the effects of the non-Newtonian behavior on flows in aneurysms is still insufficient.

Numerical simulations of flows in TOF-MRA-based cerebral aneurysm models were carried out in this study using the LBM with the SRT and the MRT models to investigate the effects of the collision model on numerical errors in the velocity fields in aneurysms. The non-Newtonian characteristics of blood was accounted for by using the Casson model. A simulation with the Newtonian viscous stress model was also carried out to investigate the effects of the viscous stress model on predicted distributions of the velocity and the wall shear stress in aneurysms.

2. Numerical Method

2.1. SRT collision model

In the lattice Boltzmann method, fluid flows are simulated by the motion of imaginary fluid particles. The distribution function, f, is a sort of the number density of particles belonging to a particle group. The number of groups is limited to Q and in the three-dimensional space the D3Q19 ($Q = 19$) discrete velocity model has often been used for isothermal incompressible flows (Fig. 1). Hence the time evolution of the discrete distribution function, f_i, of the ith particle group is calculated to predict the fluid motion, instead of solving the Navier-Stokes equation and the continuity equation. The lattice Boltzmann equation governing the time evolution of f_i is given by

$$f_i(\mathbf{x} + \mathbf{c}_i\Delta t, t + \Delta t) = f_i(\mathbf{x}, t) - \frac{f_i(\mathbf{x}, t) - f_i^{eq}(\mathbf{x}, t)}{\tau_{SRT}} \tag{1}$$

where τ_{SRT} is the relaxation time, and $\mathbf{x}$ the position vector. The time step size, Δt, is set to unity, and the equilibrium distribution functions, f_i^{eq}, are given by

$$f_i^{eq} = w_i\rho\left[1 + 3\mathbf{c}_i \cdot \mathbf{u} + \frac{9(\mathbf{c}_i \cdot \mathbf{u})^2}{2} - \frac{3\mathbf{u} \cdot \mathbf{u}}{2}\right] \tag{2}$$

where w is the weighting function given by $w_0 = 1/3$, $w_i = 1/18$ for $i = 1-6$, and $w_i = 1/36$ for $i = 7-18$ and $\mathbf{c}$ is the velocity of the particles (See Appendix). The grid spacing, Δx, is set to unity, so that particles move from a computational cell to its neighbors during Δt. The density ρ and the fluid velocity $\mathbf{u}$ are given as the moments of f_i, i.e.

$$\rho = \sum_{i=0}^{Q-1} f_i \tag{3}$$

$$\rho\mathbf{u} = \sum_{i=0}^{Q-1} \mathbf{c}_i f_i \tag{4}$$

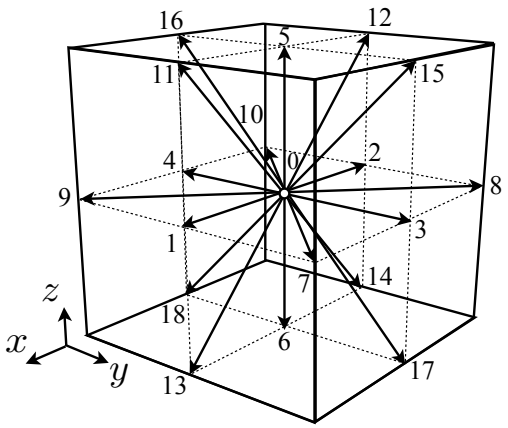

Figure 1: D3Q19 discrete velocity model (Kuzmin and Derksen, 2011)

The lattice Boltzmann equation is solved in the following two steps. First the collision step is conducted at each computational cell.

$$\tilde{f}_i(\mathbf{x}, t) = f_i(\mathbf{x}, t) - \frac{f_i(\mathbf{x}, t) - f_i^{eq}(\mathbf{x}, t)}{\tau_{SRT}} \tag{5}$$

where $\tilde{f}$ is the distribution function after the collision step (the post-collision distribution function). Then the values of $\tilde{f}$ at each computational cell are shifted to the neighboring cells in the streaming step:

$$f_i(\mathbf{x} + \mathbf{c}_i \Delta t, t + \Delta t) = \tilde{f}_i(\mathbf{x}, t) \tag{6}$$

The viscosity, μ, is given by

$$\mu = \frac{\rho}{3}\left(\tau_{SRT} - \frac{1}{2}\right) \tag{7}$$

2.2. MRT collision model

The multiple-relaxation time collision model (d'Humiéres, 2002) uses individual relaxation parameters for each moment of f. The collision process in the MRT is carried out in the moment space:

$$\mathbf{f}(\mathbf{x} + \mathbf{c}_i \Delta t, t + \Delta t) = \mathbf{f}(\mathbf{x}, t) - M^{-1} S[\mathbf{m}(\mathbf{x}, t) - \mathbf{m}^{eq}(\mathbf{x}, t)] \tag{8}$$

where $\mathbf{f}$ is the distribution function vector, whose components are f_i, and S the diagonal matrix given by

$$S = \mathrm{diag}(s_0, s_1, \cdots s_{18}) \tag{9}$$

and s_i $(i = 0 - 18)$ are the relaxation parameters. The M is the matrix transforming $\mathbf{f}$ into its moment vector $\mathbf{m}$. The components of M is given in Appendix. The $\mathbf{m}$ is therefore expressed as

$$\mathbf{m} = (\rho,\ e,\ \epsilon,\ j_x,\ q_x,\ j_y,\ q_y,\ j_z,\ q_z,\ 3p_{xx},\ 3\pi_{xx},\ p_{ww},\ \pi_{ww},\ p_{xy},\ p_{yz},\ p_{xz},\ m_x,\ m_y,\ m_z)^T \tag{10}$$

where e is the energy, ϵ the energy-squre, j_α the momentum ($\mathbf{j} = \rho\mathbf{u}$) in the α-direction, q_α the heat flux in the α-direction, $p_{\alpha\beta}$ the stress tensor components (the subscripts of the Greek letters represent tensor components in the Cartesian coordinates), π the quadratic-order moments, and m the cubic-order moments (d'Humiéres, 2002). The components of the equilibrium moment vector, $\mathbf{m}^{eq} = M\mathbf{f}^{eq}$, are given by

$$
\begin{aligned}
& e^{eq} = -11\rho + \frac{19}{\rho_0}(\mathbf{j}\cdot\mathbf{j}), \quad \epsilon^{eq} = \omega_\epsilon \rho + \frac{\omega_{\epsilon j}}{\rho_0}(\mathbf{j}\cdot\mathbf{j}), \\
& q_\alpha^{eq} = -\frac{2}{3} j_\alpha, \quad p_{xx}^{eq} = \frac{1}{\rho_0}\left(j_x^2 - \frac{\mathbf{j}\cdot\mathbf{j}}{3}\right), \\
& p_{ww}^{eq} = \frac{1}{\rho_0}\left(j_y^2 - j_z^2\right), \quad p_{xy}^{eq} = \frac{j_x j_y}{\rho_0} \\
& p_{yz}^{eq} = \frac{j_y j_z}{\rho_0}, \quad p_{xz}^{eq} = \frac{j_z j_x}{\rho_0}, \quad \pi_{xx}^{eq} = \omega_{xx} p_{xx}^{eq} \\
& \pi_{ww}^{eq} = \omega_{ww} p_{ww}^{eq}, \quad m_x^{eq} = m_y^{eq} = m_z^{eq} = 0
\end{aligned}
\tag{11}
$$

The two of s_i, i.e. s_9 and s_{13}, are related with the fluid viscosity, i.e.

$$
s_9 = s_{13} = \frac{1}{3\nu + 1/2}\left(= \frac{1}{\tau_{SRT}}\right) \tag{12}
$$

where $\nu = \mu/\rho$. The other relaxation parameters are set as follows:

$$
\begin{aligned}
& s_1 = 1.19, \quad s_2 = s_{10} = s_{12} = 1.4, \quad s_4 = s_6 = s_8 = 1.2, \\
& s_{11} = s_{14} = s_{15} = \frac{1}{\tau_{SRT}}, \quad s_{16} = s_{17} = s_{18} = 1.98
\end{aligned}
$$

The remaning parameters, $\omega_\epsilon, \omega_{\epsilon j}$ and ω_{xx}, are set to

$$
\omega_\epsilon = 3, \ \omega_{\epsilon j} = -\frac{11}{2}, \ \omega_{xx} = -\frac{1}{2}
$$

2.3. Non-Newtonian viscous stress model

The Casson model (Casson, 1959) is known to well mimic the non-Newtonian nature of human blood. The viscous stress, τ, in the Casson model is given by

$$
\tau = \begin{cases} \mu\dot{\gamma} & \text{for } |\tau| > \tau_0 \\ 0 & \text{otherwise} \end{cases} \tag{13}
$$

where $\dot{\gamma}$ is the shear rate, and μ the viscosity given by

$$
\mu = \left(\sqrt{\frac{\tau_0}{|\dot{\gamma}|}} + \sqrt{\mu_P}\right)^2 \tag{14}
$$

where τ_0 is the yield stress, and μ_P the reference viscosity. By setting $\tau_0 = 0$, the Casson model reduces to the Newtonian model with the viscosity of μ_P. The model parameters for

blood are given in Neofytou and Drikakis (2003). In numerical simulations, the following modified Casson model has often been used (Neofytou and Drikakis, 2003; Ohta et al., 2011):

$$\mu = \left(\sqrt{\frac{\tau_0}{|\dot{\gamma}|}} \left(1 - e^{-\sqrt{m|\dot{\gamma}|}} \right) + \sqrt{\mu_P} \right)^2 \tag{15}$$

where m is a constant.

The relaxation time, τ_{SRT}^{NN}, related with the fluid viscosity of a non-Newtonian fluid is calculated as

$$\tau_{SRT}^{NN} = \left(\tau_{SRT} - \frac{1}{2} \right) \left[\sqrt{\frac{Bi}{|\dot{\gamma}^*|}} \left(1 - e^{-\sqrt{m^*|\dot{\gamma}^*|}} \right) + 1 \right]^2 + \frac{1}{2} \tag{16}$$

where

$$|\dot{\gamma}^*| = \frac{|\dot{\gamma}|D}{U} \tag{17}$$

and

$$m^* = \frac{mU}{D} \tag{18}$$

Here U and D are the velocity and length scales of a flow, respectively, and Bi is the Bingham number defined by

$$Bi = \frac{\tau_0 D}{\mu_P U} \tag{19}$$

The m^* is set to 1×10^{10} (Ohta et al., 2011).

The deformation tensor $D_{\alpha\beta}$ is related with the non-equilibrium parts, $f^{(1)}$, of the distribution functions (Boyd et al., 2006):

$$D_{\alpha\beta} = -\frac{3}{2\tau_{SRT}^{NN}} \sum_i f_i^{(1)} c_{i\alpha} c_{i\beta} \tag{20}$$

where $f^{(1)}$ is given by

$$f_i^{(1)} = f_i - f_i^{eq} \tag{21}$$

The shear rate, $\dot{\gamma}_{\alpha\beta}$, in the 3D Cartesian coordinates is therefore given by

$$\dot{\gamma}_{\alpha\beta} = 2D_{\alpha\beta} \tag{22}$$

and the magnitude of the shear rate tensor is defined by

$$|\dot{\gamma}| = 2\sqrt{D_{\alpha\beta} D_{\alpha\beta}} \tag{23}$$

Note that the summation convention is applied for the subscripts of the Greek letters.

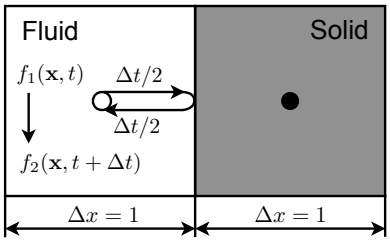

Figure 2: Half-way bounce-back scheme

2.4. Interpolated bounce-back scheme

One of the advantages of the LBM is the easy implementation of the no-slip boundary condition at solid walls. Fig. 2 shows a computational cell containing the fluid phase neighboring to that of the solid phase. The particles in the group of f_1 travel from the cell center toward the wall during $\Delta t/2$, and then, go back to the fluid region after the collision with the wall. They return to the cell center at $t + \Delta t$. Since the direction of the motion of the particles changed from 1 to 2,

$$\tilde{f}_2(\mathbf{x}, t + \Delta t) = \tilde{f}_1(\mathbf{x}, t) \tag{24}$$

This is called the half-way bounce-back scheme.

Pan et al. (2006) extended the half-way bounce-back scheme for arbitrary curved boundaries. When $q < 1/2$, the following interpolation is used to obtain the distribution function after the bounce-back process:

$$\tilde{f}_{\bar{i}}(\mathbf{x}, t + \Delta t) = 2q_i \tilde{f}_i(\mathbf{x}, t) + (1 - 2q_i)\tilde{f}_i(\mathbf{x} - \mathbf{c}_i \Delta t, t) \tag{25}$$

where q_i is the distance between a computational cell and the wall in the ith direction as shown in Fig. 3(a), and the bar represents the opposite direction of i, e.g. $\bar{i} = 2$ for $i = 1$. When $q \geq 1/2$, the distribution function is obtained by using the following extrapolation function (Fig. 3(b)):

$$\tilde{f}_{\bar{i}}(\mathbf{x}, t + \Delta t) = \frac{1}{2q_i}\tilde{f}_i(\mathbf{x}, t) + \left(\frac{2q_i - 1}{2q_i}\right)\tilde{f}_{\bar{i}}(\mathbf{x}, t) \tag{26}$$

2.5. Cerebral aneurysm modeling

DICOM (digital imaging and communications in medicine) data acquired by TOF-MRA (Achieva 1.5T Nova Dual, Philips; Achieva 3.0T TX Quasar Dual, Philips; Ingenia 3.0T R5.1.7, Philips; Taitan 3T, Toshiba Medical Systems) are used to simulate fluid flows in cerebral aneurysms. OsiriX (Pixmeo), a DICOM imaging viewer, is used to extract aneurysms. The DICOM data are imported into OsiriX, whose surface rendering function is applied to the data to capture aneurysms and to export the surface data as STL (standard triangulated language) meshes, where the STL mesh is a set of triangles orientated by unit normals.

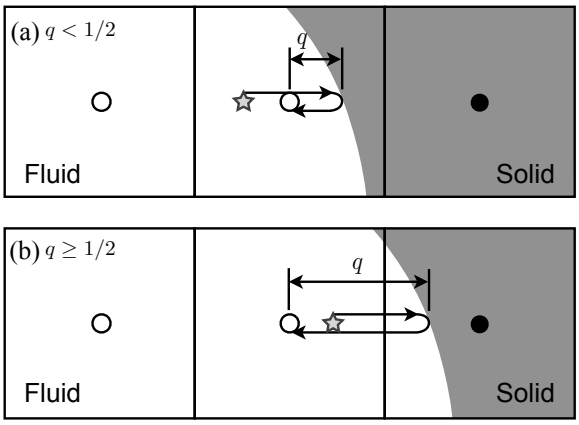

Figure 3: Interpolated bounce-back scheme (Pan et al., 2006)

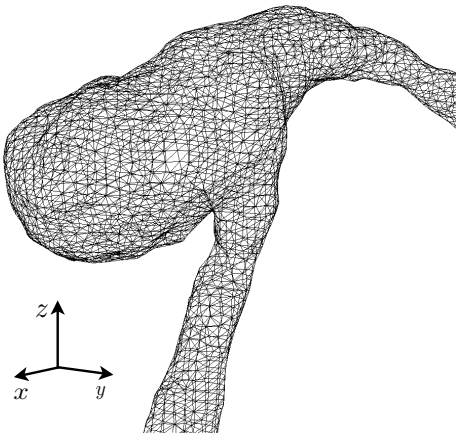

Figure 4: Aneurysm model extracted from TOF-MRA DICOM data

The STL mesh data are imported into our in-house LBM code and are used to reconstruct the level set function, ψ, which is used to evaluate the distance fraction, q, in the interpolated bounce-back scheme. The ψ is the positive distance from the wall to a position in the solid phase region and is the negative distance in the fluid phase region, and therefore, the zero-level set, $\psi = 0$, is the wall. The ψ is reconstructed from the STL mesh data using the method given in our previous study (Hayashi et al., 2006) as follows. For the Cth computational cell at $\mathbf{x}_C$, the distance from the wall given by the eth triangular element is given by

$$\psi^L_{e\to C} = (\mathbf{x}_C - \mathbf{x}_e) \cdot \mathbf{n}_e \tag{27}$$

where $\mathbf{x}_e$ and $\mathbf{n}_e$ are the position vector and the unit normal, respectively, of the eth element. Contributions from all the elements near $\mathbf{x}_C$ are collected to obtain $\psi(\mathbf{x}_C)$ using the following weighting average:

$$\psi(\mathbf{x}_C) = \frac{\sum_e \psi^L_{e\to C} |\mathbf{x}_C - \mathbf{x}_e|^{-p}}{\sum_e |\mathbf{x}_C - \mathbf{x}_e|^{-p}} \tag{28}$$

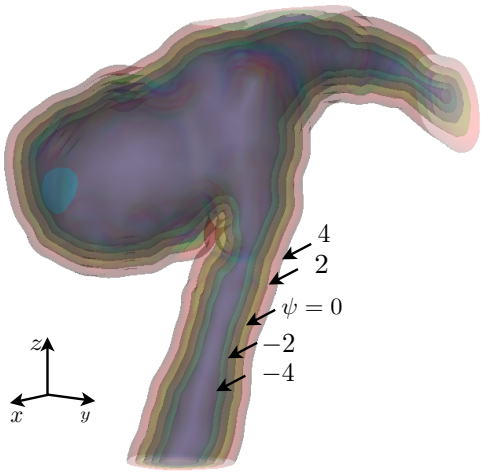

Figure 5: Level set function for aneurysm surface representation (color online)

where the power, p, for the weight is set to seven. Fig. 5 shows an example of the reconstructed level set functions. This procedure does not need to solve the partial differential equation, $\partial\psi/\partial t = \mathrm{sign}(\psi)(|\nabla\psi| - 1)$ (Sussman et al., 1994; He et al., 2009), to assure the property of the distance function, $|\nabla\psi| = 1$.

By making use of ψ, q_i are given by

$$q_i = \frac{|\psi(\mathbf{x})|}{|\psi(\mathbf{x})| + |\psi(\mathbf{x} + \mathbf{c}_i\Delta t)|} \tag{29}$$

2.6. Code development and CPU times of relaxation time models

The locality of the collision process, i.e. all the variables required for the particle collision at a computational cell locate at the same cell, is suitable for parallel computing. This is one of the attractive advantages of the LBM and the reason why many researchers have been applying GPGPU (general-purpose computing on graphics processing units) to LB simulations. Two Tesla-type GPU boards embedded in a single workstation were used and they worked in parallel by means of the block-division method. Validations of the developed numerical code were carried out for Newtonian and non-Newtonian fluid flows in a circular pipe, between parallel flat walls and in a square cavity. The results agreed with the analytical (Ohta et al., 2011) and well-accepted numerical results (Neofytou, 2005). The CPU times in the simulations of the cerebral aneurysms were measured (see Section 3 for detail). It should be noted that the LBM was simply coded and no special optimizations were carried out in the present study. The CPU times in the MRT were three times longer than that of the SRT in all the cases.

3. Numerical Condition

Models of cerebral arteries used in the present study are shown in Fig. 6. Hereafter, they are referred to as Case 1-4. The aneurysm of Case 1 is an anterior communicating artery

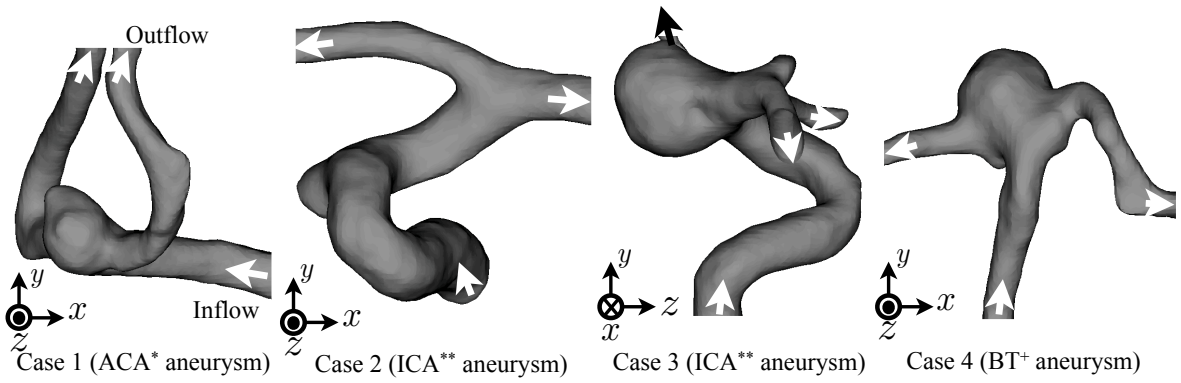

Figure 6: Cerebral artery models reconstructed from TOF-MRA data (Contour surfaces of $\psi = 0$). *ACA: anterior communicating artery, **ICA: internal carotid artery, +BT: basilar tip

aneurysm and that of Case 4 is a basilar tip aneurysm. The aneurysms in Case 2 and 3 are a left and a right internal carotid artery aneurysm, respectively.

The pulsation of a blood flow was neglected, i.e. the flow was assumed to be steady, to focus on the effects of the collision models on the numerical accuracy and stability, although the numerical method can deal with unsteady blood flows (Kimura et al., 2019a).

Hence the dimensionless groups governing the flow are the Bingham number defined by Eq. (19) and the Reynolds number, Re, defined by

$$Re = \frac{\rho U D}{\mu_P} \tag{30}$$

The characteristic length scales, D, of Bi and Re are given as the circle-area-equivalent inlet diameter. As for the typical values of Re and Bi, $Re = 200$ and $Bi = 0.1$ were used (Yamaguchi, 2008; Neofytou and Drikakis, 2003). The simulation was also carried out with $Bi = 0$ (Newtonian fluid) to discuss the effects of Bi on the flow in the cerebral aneurysm.

The uniform velocity distribution was imposed on the inflow boundary. The pressure was fixed at a reference value and the velocity gradient was set to zero at the outflow boundaries. The characteristic velocity, U, was set at 0.02 in all the simulations to ensure the incompressible condition in the LB scheme. The spatial resolutions in each case are shown in Table 1, where the numbers of the cells are for the whole domain. Resolution 1 and Resolution 2 are the low and high spatial resolution conditions, respectively, and the latter is twice as high as the former. Ratios of the number of cells inside the arteries (fluid region) to that for the whole domain were 0.055, 0.010, 0.09 and 0.051 in Case 1, 2, 3 and 4, respectively. For example, 202,752 cells were used to cover the whole rectangular domain in Case 2 of Resolution 1, whereas 20,200 cells were fluid cells. The number of fluid cells was 161,600 for Resolution 2. The circle-area-equivalent diameters, D, of the inlet arteries were 11.3, 16.4, 11.1 and 7.7 cells in Case 1, 2, 3 and 4 for Resolution 1. The diameters of the outlet arteries were comparable to or smaller than those of the inlet arteries, e.g. the circle-area-equivalent diameters of the two outlets in Case 1 of Resolution 1 were 9.0 and

Table 1: Numbers of computational cells, (N_x, N_y, N_z), in each direction

Case	Resolution 1	Resolution 2
1	$(64, 63, 74)$	$(128, 125, 148)$
2	$(64, 66, 48)$	$(128, 131, 96)$
3	$(64, 62, 58)$	$(128, 123, 114)$
4	$(64, 62, 56)$	$(128, 123, 112)$

7.9 cells. The calculation times taken for 10,000 time steps were, for example, 0.28, 0.2, 0.22 and 0.21 hour in Case 1, 2, 3 and 4 with the SRT and Resolution 1.

4. Results and Discussion

4.1. Flow structure

Fig. 7(a) shows streamlines of the flow fields predicted using the MRT. The blood flows from the right side of the main artery toward the cerebral aneurysm, in which a swirl-like vortical structure is formed due to the collision between the flow and the aneurysm wall. Then the blood flows out from the aneurysm to the branches. Streamlines in Case 2 are shown in Fig. 7(b). In this case, the cerebral aneurysm forms on the side wall of the winding main artery. The blood coming from the inlet directly flows to the connection with the branches. Some amount of the blood is however flowing into the aneurysm and forms a vortical flow structure inside it. The vortical structures forming in the aneurysms of Case 3 and 4 (Fig. 7(c) and (d)) are as large as the aneurysms, and the magnitudes of the velocities close to the aneurysm walls are much smaller than U.

The flow structures predicted using the SRT at Resolution 1 were similar to those using the MRT (figures are omitted to conserve space) except for Case 4. The simulation of Case 4 using the SRT was unstable, so that we could not obtain its steady state solution. The increase in the spatial resolution up to Resolution 2 was required to obtain the steady state solution.

4.2. Flow filed in aneurysm

Fig. 8 shows the velocity field at a cross section of the aneurysm in Case 1. The velocity field of the SRT (a) is almost the same as that of the MRT (b), and both collision models predict the vortical structure flowing smoothly along the aneurysm wall. The velocity fields in Case 2 shown in Fig. 9 are also smooth and no remarkable differences are observed. The increase in the spatial resolution has a little influence on the flow structure in these cases.

The MRT gives a smooth velocity profile also in Case 3 as shown in Fig. 10(b), whereas the velocities in the box represented by the dotted line in the SRT (a) are disturbed (See its magnified view in Fig. 11(a)). In the SRT, several velocities in computational cells of the nearest neighbors of the aneurysm wall are much larger than those in the MRT and toward the wall, implying that the boundary condition of the zero velocity normal to the wall is deteriorated due to numerical errors. Unphysical streamlines penetrating into the solid

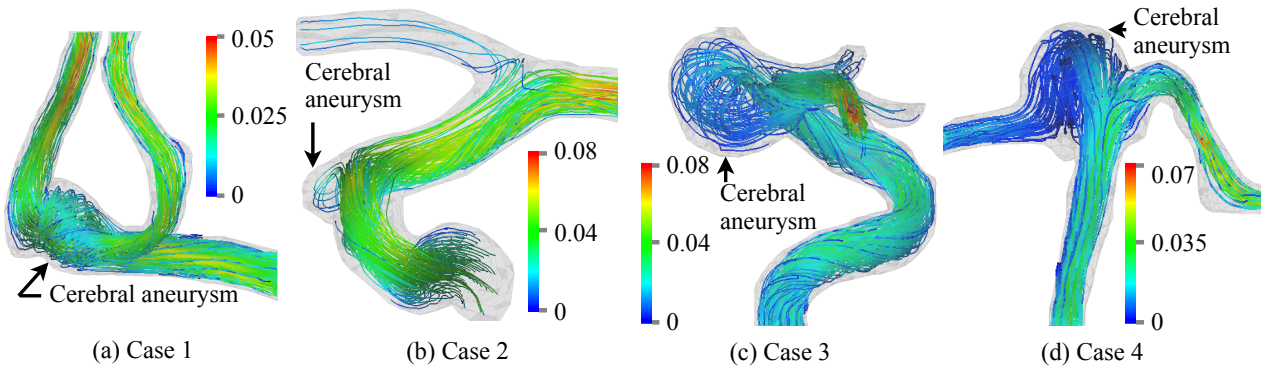

Figure 7: Streamlines (MRT; Resolution 1) (Color represents magnitude of velocity) (color online)

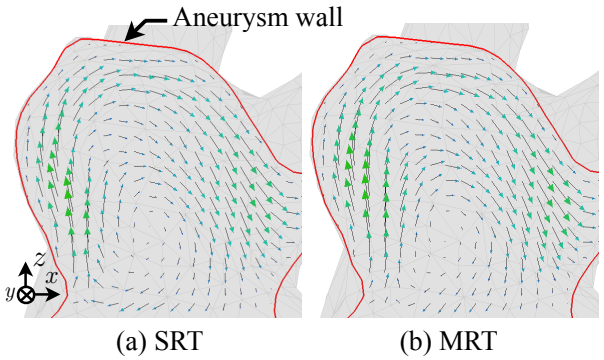

Figure 8: Velocity field at cross section of aneurysm (Case 1, Resolution 1. Vectors are colored with the same color bar in Fig. 7)

region can also be observed in the LB simulation with the SRT reported in Weichert et al. (2013) although they did not remark this point. In cerebral aneurysms, the fluid velocity is apt to be much smaller than in the main artery. The small velocity scale in the aneurysm can be the cause of the numerical errors in the vicinity of the wall in the SRT. The MRT successfully removes the velocity error (Fig. 11(b)).

The unphysical velocity distribution due to numerical errors in the SRT case could be suppressed at Resolution 2 and the result was almost the same as that of the MRT (a figure of this result is omitted to conserve space). Resolution 2 in Case 4 also made it possible to stably simulate the flow even with the SRT as shown in Fig. 12. The flow structure in the aneurysm predicted with the SRT agrees with that with the MRT. However the velocity distribution close to the aneurysm wall possesses some numerical errors as shown in Fig. 13, implying that, when SRT is used, further increase in the spatial resolution would be needed to sufficiently decrease the numerical errors.

The numerical error in the velocity is apt to occur in small velocity regions close to the walls. Even though the magnitude of the velocity error is much smaller than the mean

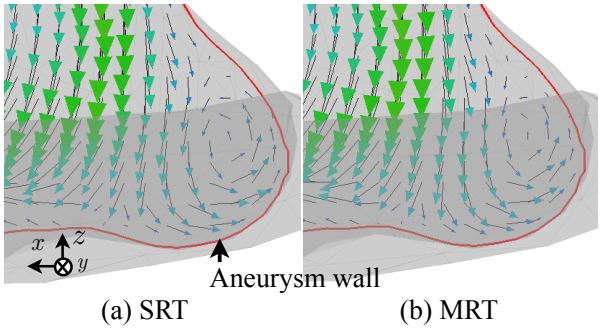

Figure 9: Velocity field at cross section of aneurysm (Case 2, Resolution 1. Vectors are colored with the same color bar in Fig. 7)

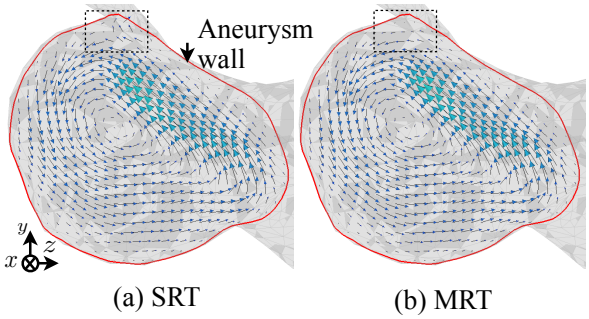

Figure 10: Velocity field at cross section of aneurysm (Case 3. Resolution 1. Vectors are colored with the same color bar in Fig. 7)

velocity in the aneurysm, it may affect the evaluation of the wall shear stress, τ_W, which has been considered as one of the most important hemodynamic factors in the growth and/or the rupture of aneurysms. By making use of ψ, τ_W at a computational cell neighboring to the wall was evaluated as

$$\tau_W = |(\mathbf{I} - \mathbf{nn}) \cdot (\mu \nabla \mathbf{u})| \approx \left| \mu \frac{(\mathbf{I} - \mathbf{nn}) \cdot \mathbf{u}(\mathbf{x})}{\psi(\mathbf{x})} \right| \tag{31}$$

where $\mathbf{I}$ is the unit tensor, and $\mathbf{n}$ the unit normal to the interface given by

$$\mathbf{n} = \frac{\nabla \psi}{|\nabla \psi|} \tag{32}$$

Fig. 14 shows the wall shear stress, $\widetilde{\tau_W} (= \tau_W/(\rho U^2/2))$, scaled by the dynamic pressure $\rho U^2/2$. In the MRT, the cross-sectional-averaged wall shear stress, $< \widetilde{\tau_W} >^w$, and the mean wall shear stress, $< \widetilde{\tau_W} >^l$, in the region surrounded by the dotted-line box (Fig. 12) are 0.024 and 0.0081, respectively. The mean shear stress in the SRT ($< \widetilde{\tau_W} >^w = 0.028$) is 14% larger than the MRT. In addition, $< \widetilde{\tau_W} >^l$ is 0.038, which is much larger than in the MRT. The larger $\widetilde{\tau_W}$ in the SRT is attributed to the velocity errors in the near wall region. These results suggest that we should be careful in evaluating τ_W when the SRT is utilized.

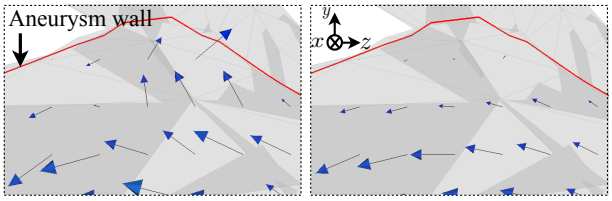

Figure 11: Magnified views of velocity fields in Case 3

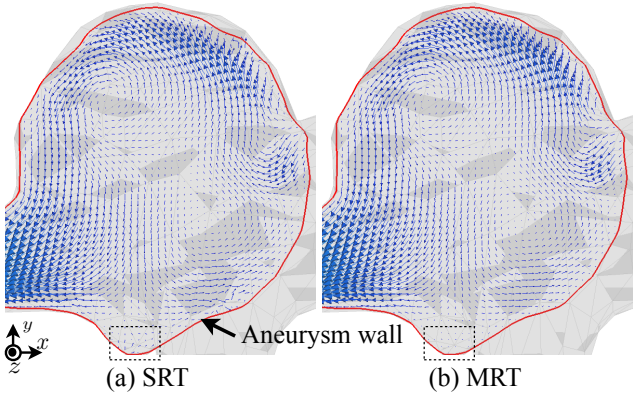

Figure 12: Velocity field at cross section of aneurysm (Case 4; Resolution 2. Vectors are colored with the same color bar in Fig. 7)

4.3. Two-relaxation time collision model

Although the MRT can give better numerical stability and accuracy than the SRT, the moment-based calculation is more time consuming and trial-and-error simulations may be required to find the optimal values of the free parameters. A collision model having a fewer number of free parameters would be of use in practice. Therefore the applicability of the two-relaxation time (TRT) collision model (Ginzburg et al., 2008, 2010; Seta et al., 2014, 2018), in which one relaxation parameter is used to determine the fluid viscosity and the other is a free parameter used to improve numerical stability and accuracy, is examined in this section.

The lattice Boltzmann equation with the TRT is given by

$$f_i(\mathbf{x}+\mathbf{c}_i\Delta t, t+\Delta t) = f_i(\mathbf{x},t) - \frac{f_i^+(\mathbf{x},t) - f_i^{+,eq}(\mathbf{x},t)}{\tau_+} - \frac{f_i^-(\mathbf{x},t) - f_i^{-,eq}(\mathbf{x},t)}{\tau_-} \tag{33}$$

where the symmetric and the asymmetric parts, f_i^+ and f_i^-, of f_i are defined by

$$f_i^+ = \frac{f_i + f_{\bar{i}}}{2}, \quad f_i^- = \frac{f_i - f_{\bar{i}}}{2} \tag{34}$$

$$f_i^{+,eq} = \frac{f_i^{eq} + f_{\bar{i}}^{eq}}{2}, \quad f_i^{-,eq} = \frac{f_i^{eq} - f_{\bar{i}}^{eq}}{2} \tag{35}$$

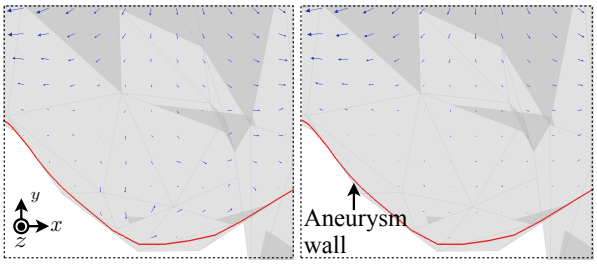

Figure 13: Magnified views of velocity fields in Case 4 (Resolution 2)

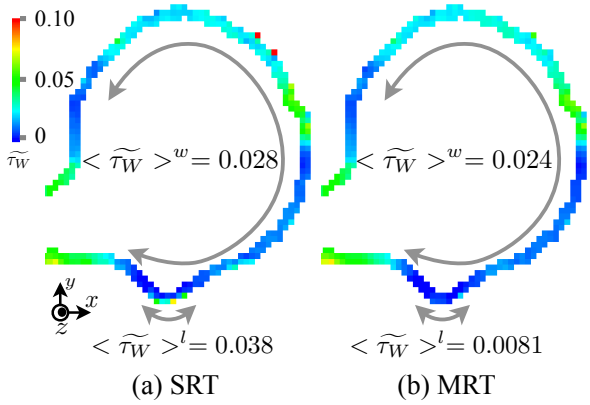

Figure 14: Wall shear stress $\widetilde{\tau_W}(= \tau_W/(\rho U^2/2))$ (color online)

and $\bar{i}$ denotes the direction opposite to i. The relaxation time, τ_+, for the symmetric part is related with the fluid viscosity and is given by

$$\tau_+ = \tau_{SRT}^{NN} \tag{36}$$

The relaxation time, τ_-, for the asymmetric part is a free parameter and can be used to improve the numerical accuracy and stability. The following parameter is often used to set τ_-:

$$\Lambda = \left(\tau_+ - \frac{1}{2}\right)\left(\tau_- - \frac{1}{2}\right) \tag{37}$$

The numerical stability with the typical values of Λ, i.e. $\Lambda = 1/4,\ 3/16,\ 1/6$ and $1/12$ (Ginzburg et al., 2008, 2010), were first examined. As shown in Table 2, the simulations were unstable with these Λ. Although Λ was decreased down to $1/100$, a stable result could not be obtained. However further reduction of Λ made the simulation stable and conditions of $\Lambda \leq 1/200$ gave steady state solutions as shown in the table. The velocity distribution in the aneurysm at $\Lambda = 1/200$ is shown in Fig. 15(a). The comparison between the prediction with the TRT and that of the SRT clearly shows that the TRT improves the numerical accuracy in the near wall region.

Table 2: Effects of Λ on numerical stability in TRT simulations (Case 3, Resolution 1. N: No, Y: Yes)

Λ	1/4	3/16	1/6	1/12	1/100	1/200	1/400	$1/10^4$
Stable	N	N	N	N	N	Y	Y	Y

Table 3: Effects of Λ on numerical stability in TRT simulations (Case 4, Resolution 2. N: No, Y: Yes)

Λ	1/4	3/16	1/6	1/12	1/20	1/40	1/100	1/200
Stable	N	N	N	N	N	Y	Y	Y

In Case 4 at Resolution 1, the stabilization was not sufficient to obtain a steady state solution even with the TRT. Steady state solutions could be obtained with Resolution 2 by using Λ for $\Lambda \leq 1/40$ as shown in Table 3. The accuracy of the TRT is better than the SRT and comparable to the MRT as shown in Fig. 15(b).

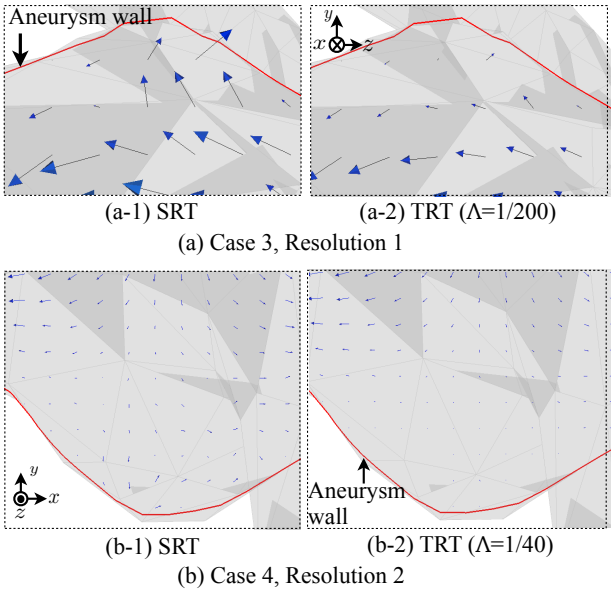

Figure 15: Comparison between velocity fields predicted using SRT and TRT

Although the TRT is less stable than the MRT, it can achieve better accuracy than the SRT and the predicted velocity profiles in the aneurysms are almost the same as those obtained by the MRT.

4.4. Effects of viscous stress model

Fig. 16 shows velocity fields in the cerebral aneurysms predicted using the Newtonian viscous stress model, i.e. $Bi = 0$. Here the collision model is MRT and the spatial resolution

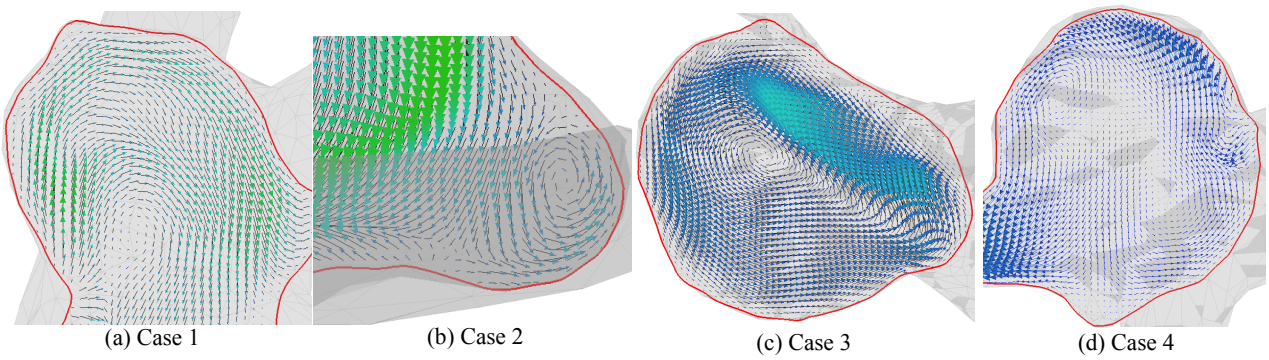

Figure 16: Velocity fields in cerebral aneurysms at $Bi = 0$ (Newtonian fluid) (color online)

is Resolution 2. From the point of view of the flow structure, no remarkable differences from the non-Newtonian cases (Figs. 8-12) are observed.

Fig. 17 shows comparisons between $\widetilde{\tau}_W$ at $Bi = 0.1$ and 0. The distributions are not so different from the qualitative point of view. Table 4 summarizes the values of $\widetilde{\tau}_W$ to quantitatively investigate the Bi effects on $\widetilde{\tau}_W$. The mean $\widetilde{\tau}_W$ is $\widetilde{\tau}_W$ averaged for the whole aneurysm region, i.e. $< \widetilde{\tau}_W >^w$, $\max(\widetilde{\tau}_W)$ is the maximum value of $\widetilde{\tau}_W$ in the aneurysm, and $\min(\widetilde{\tau}_W)$ is the minimum value of $\widetilde{\tau}_W$. The changes in $\widetilde{\tau}_W$ with decreasing Bi are also shown in the table. The decrease in Bi down to 0 causes 9% reduction in $< \widetilde{\tau}_W >^w$ in Case 1. On the other hand, in Case 2, the change in $< \widetilde{\tau}_W >^w$ is very small. In Case 3, $< \widetilde{\tau}_W >^w$ shows 6% difference. Although the difference in the minimum value is 15%, the maximum $\widetilde{\tau}_W$ is almost the same. The largest difference in $< \widetilde{\tau}_W >^w$ is found in Case 4, i.e. 12% reduction. In this case, the changes in $\max(\widetilde{\tau}_W)$ and $\min(\widetilde{\tau}_W)$ are also large.

The effects of Bi on $\widetilde{\tau}_W$ are small only in Case 2. In this case, the aneurysm forms on the side wall of the main artery and the flow does not directly flow into the aneurysm. On the other hand, in the other three cases, the aneurysms form at the bifurcations from the main arteries to their branches and the flows coming from the main arteries form vortical structures in the aneurysms and then go out to the branches. Interestingly the wall shear stress tends to increase with decreasing Bi only in Case 2. Therefore the Bi effect on $\widetilde{\tau}_W$ depends on the configuration of the aneurysm and the flow direction, although the number of samples used here is small.

In summary, the Bingham number does not have a large influence on the structures of the flows in the cerebral aneurysms within the present Bi range, i.e. $Bi = 0 - 0.1$. However, from the point of view of the wall shear stress, the mean wall shear stress may change over several percent by neglecting the non-Newtonian nature of blood. Especially, when focusing on the local wall shear stress, the use of the Newtonian viscous stress model can lead to a wall shear stress largely different from that with the Casson model.

Table 4: Comparisons of $\widetilde{\tau}_W$ between Casson and Newtonian fluids. Changes in τ_W defined by $[\tau_W(Bi = 0) - \tau_W(Bi = 0.1)]/\tau_W(Bi = 0.1)$ are also given in the third rows in each case.

Case	Bi	Mean $\widetilde{\tau}_W$	max($\widetilde{\tau}_W$)	min($\widetilde{\tau}_W$)
1	0.1	0.121	0.33	0.0054
	0.0	0.110	0.29	0.0029
		-9.1%	-14%	-46%
2	0.1	0.175	0.42	0.029
	0.0	0.176	0.42	0.034
		0.5%	0.7%	15%
3	0.1	0.047	0.10	0.0082
	0.0	0.044	0.10	0.0050
		-6.0%	0%	-39%
4	0.1	0.024	0.077	0.0021
	0.0	0.021	0.066	0.00057
		-12%	-14%	-73%

5. Conclusion

Lattice Boltzmann simulations of flows in cerebral aneurysms were carried out using three collision models, i.e. the single-relaxation time model (SRT), the two-relaxation time model (TRT) and the multiple-relaxation time model (MRT), to investigate the effects of the collision model on the predictions. Four cerebral aneurysm models were used in the simulation. The shapes of cerebral arteries were extracted from TOF-MRA data as STL meshes, and the level set function (signed-distance function) representing the artery wall was reconstructed from the STL mesh data based on the reconstruction method proposed by Hayashi et al. (2006). By making use of the level set function in the interpolated bounce-back scheme, the complex structures of arteries having aneurysms could be easily dealt with. The Casson model was utilized to account for the non-Newtonian viscous stress. The conclusions obtained are as follows:

1. The SRT can give reasonable predictions comparable to the MRT, provided that the spatial resolution is high enough, otherwise numerical errors can be large and numerical instabilities take place.
2. Velocity errors are apt to take place in the near aneurysm wall region due to a small velocity scale.
3. Although the TRT is less stable than the MRT, predictions of the TRT under stable numerical conditions are almost the same as those of the MRT.
4. The Bingham number effect on the flow structure is small. The mean wall shear stress, however, may change over several percent, depending on the configuration of the aneurysm and the main blood flow, by neglecting the non-Newtonian nature of blood.

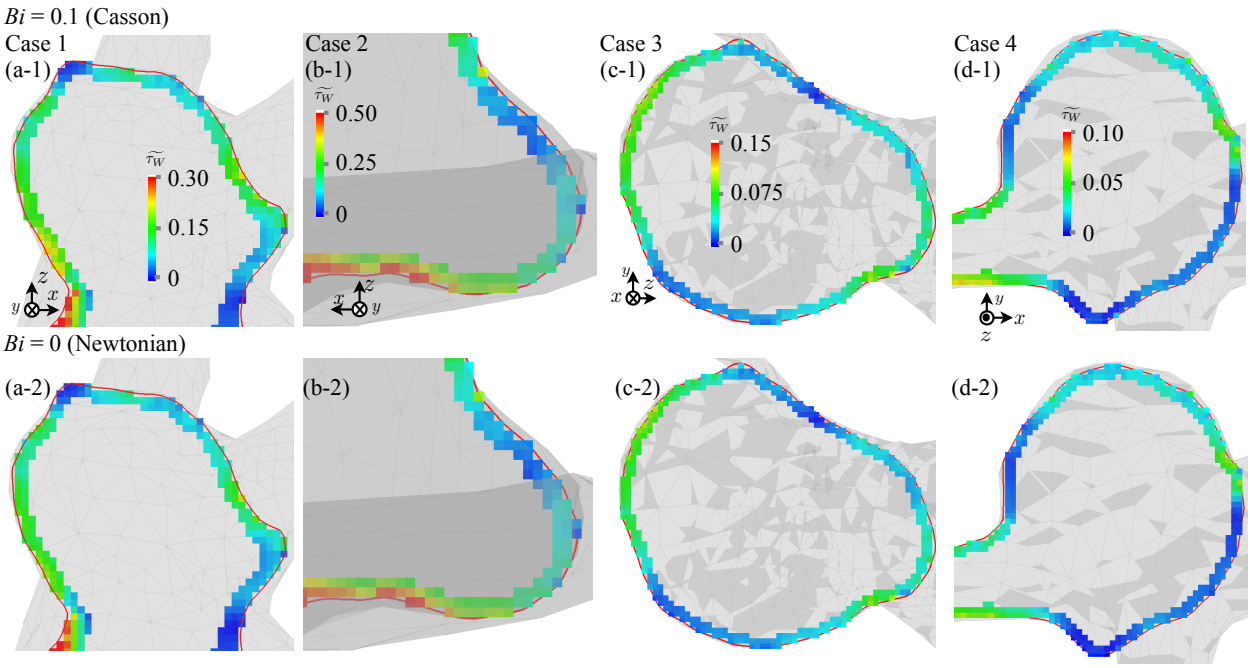

Figure 17: Wall shear stresses, τ_W, at $Bi = 0.1$ (Casson fluid) and $Bi = 0$ (Newtonian fluid) (color online)

Acknowledgement

This work has been supported by JSPS KAKENHI Grant Number 17K10826.

Appendix A. Lattice velocity and transformation matrix in MRT

The components of the lattice velocity, $\mathbf{c}$, in the D3Q19 model are given by

$$\begin{pmatrix} c_{x0} & c_{x1} & \cdots & c_{x18} \\ c_{y0} & c_{y1} & \cdots & c_{y18} \\ c_{z0} & c_{z1} & \cdots & c_{z18} \end{pmatrix} = \begin{pmatrix} 0 & 1 & -1 & 0 & 0 & 0 & 0 & 1 & -1 & 1 & -1 & 1 & -1 & 1 & -1 & 0 & 0 & 0 & 0 \\ 0 & 0 & 0 & 1 & -1 & 0 & 0 & 1 & 1 & -1 & -1 & 0 & 0 & 0 & 0 & 1 & -1 & 1 & -1 \\ 0 & 0 & 0 & 0 & 0 & 1 & -1 & 0 & 0 & 0 & 0 & 1 & 1 & -1 & -1 & 1 & 1 & -1 & -1 \end{pmatrix} \tag{A.1}$$

The transformation matrix M in the MRT is given by

$$M = \begin{pmatrix} 1 & 1 & 1 & 1 & 1 & 1 & 1 & 1 & 1 & 1 & 1 & 1 & 1 & 1 & 1 & 1 & 1 & 1 & 1 \\ -30 & -11 & -11 & -11 & -11 & -11 & -11 & 8 & 8 & 8 & 8 & 8 & 8 & 8 & 8 & 8 & 8 & 8 & 8 \\ 12 & -4 & -4 & -4 & -4 & -4 & -4 & 1 & 1 & 1 & 1 & 1 & 1 & 1 & 1 & 1 & 1 & 1 & 1 \\ 0 & 1 & -1 & 0 & 0 & 0 & 0 & 1 & -1 & 1 & -1 & 1 & -1 & 1 & -1 & 0 & 0 & 0 & 0 \\ 0 & -4 & 4 & 0 & 0 & 0 & 0 & 1 & -1 & 1 & -1 & 1 & -1 & 1 & -1 & 0 & 0 & 0 & 0 \\ 0 & 0 & 0 & 1 & -1 & 0 & 0 & 1 & 1 & -1 & -1 & 0 & 0 & 0 & 0 & 1 & -1 & 1 & -1 \\ 0 & 0 & 0 & -4 & 4 & 0 & 0 & 1 & 1 & -1 & -1 & 0 & 0 & 0 & 0 & 1 & -1 & 1 & -1 \\ 0 & 0 & 0 & 0 & 0 & 1 & -1 & 0 & 0 & 0 & 0 & 1 & 1 & -1 & -1 & 1 & 1 & -1 & -1 \\ 0 & 0 & 0 & 0 & 0 & -4 & 4 & 0 & 0 & 0 & 0 & 1 & 1 & -1 & -1 & 1 & 1 & -1 & -1 \\ 0 & 2 & 2 & -1 & -1 & -1 & -1 & 1 & 1 & 1 & 1 & 1 & 1 & 1 & 1 & -2 & -2 & -2 & -2 \\ 0 & -4 & -4 & 2 & 2 & 2 & 2 & 1 & 1 & 1 & 1 & 1 & 1 & 1 & 1 & -2 & -2 & -2 & -2 \\ 0 & 0 & 0 & 1 & 1 & -1 & -1 & 1 & 1 & 1 & 1 & -1 & -1 & -1 & -1 & 0 & 0 & 0 & 0 \\ 0 & 0 & 0 & -2 & -2 & 2 & 2 & 1 & 1 & 1 & 1 & -1 & -1 & -1 & -1 & 0 & 0 & 0 & 0 \\ 0 & 0 & 0 & 0 & 0 & 0 & 0 & 1 & -1 & -1 & 1 & 0 & 0 & 0 & 0 & 0 & 0 & 0 & 0 \\ 0 & 0 & 0 & 0 & 0 & 0 & 0 & 0 & 0 & 0 & 0 & 0 & 0 & 0 & 0 & 1 & -1 & -1 & 1 \\ 0 & 0 & 0 & 0 & 0 & 0 & 0 & 0 & 0 & 0 & 0 & 1 & -1 & -1 & 1 & 0 & 0 & 0 & 0 \\ 0 & 0 & 0 & 0 & 0 & 0 & 0 & 1 & -1 & 1 & -1 & -1 & 1 & -1 & 1 & 0 & 0 & 0 & 0 \\ 0 & 0 & 0 & 0 & 0 & 0 & 0 & -1 & -1 & 1 & 1 & 0 & 0 & 0 & 0 & 1 & -1 & 1 & -1 \\ 0 & 0 & 0 & 0 & 0 & 0 & 0 & 0 & 0 & 0 & 0 & 1 & 1 & -1 & -1 & -1 & -1 & 1 & 1 \end{pmatrix} \tag{A.2}$$

References

Ashrafizaadeh, M., Bakhshaei, H., 2009. A comparison of non-Newtonian models for lattice Boltzmann blood flow simulations. Computers and Mathematics with Applications 58, 1045–1054.

Bernsdorf, J., Wang, D., 2009. Non-Newtonian blood flow simulation in cerebral aneurysms. Computers and Mathematics with Applications 58, 1024–1029.

Boyd, J., Buick, J., Green, S., 2006. A second-order accurate lattice boltzmann non-newtonian flow model. Journal of Physics A: Mathematical and General 39, 14241–14247.

Boyd, J., Buick, J., Green, S., 2009. Analysis of the Casson and Crreau-Yasuda non-Newtonian blood model in steady and oscillatory flows using the lattice Boltzmann method. Physics of Fluids 19(9), 093103.

Carreau, P. J., 1972. Rheological equation from molecular theories. Transactions of the Society of Rheology 147, 99–127.

Casson, N. A., 1959. A flow equation for pigment-oil suspension of the printing ink type. Pergamon Press, New York, pp. 84–104.

Cebral, J. R., Castro, M. A., Appanaboyina, S., Putman, C. M., Millan, D., Frangi, A. F., 2005. Efficient pipeline for image-based patient-specific analysis of cerebral aneurysm hemodynamics: Technique and sensitivity. IEEE Transactions on Medical Imaging 24(4), 457–467.

Chen, S., Doolen, G. D., 1998. Lattice boltzmann method for fluid flows. Annual Review of Fluid Mechanics 30, 329–364.

d'Humiéres, D., 2002. Multiple-relaxation-time lattice Boltzmann models in three dimensions. Philosophical Transactions of the Royal Society of London. Series A:Mathematical, Physical and Engineering Sciences 360, 437–451.

Gabbanelli, S., Drazer, G., Koplik, J., 2005. Lattice Boltzmann method for non-Newtonian (power-law) fluids. Physical Review E 72, 046312.

Ginzburg, I., d'Humiéres, D., Kuzmin, A., 2010. Optimal stability of advection-diffusion lattice Boltzmann models with two relaxation times for positive/negative equilibrium. Journal of Statistical Physics 139(6), 1090–1143.

Ginzburg, I., Verhaeghe, F., d'Humiéres, D., 2008. Two-relaxation-time lattice Boltzmann scheme: About parametrization, velocity, pressure and mixed boundary conditions. Communications in Computational Physics 3(2), 427–478.

Hayashi, K., Sou, A., Tomiyama, A., 2006. A volume tracking method based on non-uniform subcells and continuum surface force model using a local level set function. Computational Fluids Dynamics Journal 15(2), 225–232.

He, X., Duckwiler, G., Valentino, D. J., 2009. Lattice Boltzmann simulation of cerebral artery hemodynamics. Computers & Fluids 38, 789–796.

Huang, C., Chai, Z., Shi, B., 2013. Non-Newtonian effect on hemodynamic characteristics of blood flow in stented cerebral aneurysm. Communications in Computational Physics 13(3), 916–928.

Kim, Y. H., Xu, X., Lee, J. S., 2010. The effect of stent porosity and strut shape on saccular aneurysm and its numerical analysis with lattice Boltzmann method. Annals of Biomedical Engineering 38, 2274–2292.

Kimura, H., Hayashi, K., Taniguchi, M., Hosoda, K., Fujita, A., Seta, T., Tomiyama, A., Kohmura, E., 2019a. Detection of hemodynamic characteristics before growth in growing cerebral aneurysms by analyzing time-of-flight magnetic resonance angiography images alone: preliminary results. World Neurosurgery 122, e1439–e1448.

Kimura, H., Taniguchi, M., Hayashi, K., Fujimoto, Y., Fujita, Y., Sasayama, T., Tomiyama, A., 2019b. Clear detection of thin-walled regions in unruptured cerebral aneurysms by using computational fluid dynamics. World Neurosurgery 121, e287–e295.

Kuzmin, A., Derksen, J., 2011. Introduction to the lattice Boltzmann method. In: LBM Workshop. Edmonton.

Lou, Z., Yang, W.-J., 1993. A computer simulation of the non-Newtonian blood flow at the aortic bifurcation. Journal of Biomechanics 26(1), 37–49.

Neofytou, P., 2005. A 3rd order upwind finite volume method for generalised Newtonian fluid flows. Advances in Engineering Software 36(10), 664–680.

Neofytou, P., Drikakis, D., 2003. Non-Newtonian flow instability in a channel with a sudden expansion. Journal of Non-Newtonian Fluid Mechanics 111, 127–150.

Ohta, M., Nakamura, T., Yoshida, Y., Matsukuma, Y., 2011. Lattice Boltzmann simulations of viscoplastic fluid flows through complex flow channels. Journal of Non-Newtonian Fluid Mechanics 166, 404–412.

Oshima, M., Sakai, H., Torii, R., 2005. Modelling of infow boundary conditions for image-based simulation of cerebrovascular flow. International Journal of Numerical Methods in Fluids 47, 603–617.

Pan, C., Luo, L., Miller, C., 2006. An evaluation of lattice boltzmann schemes for porous medium flow simulation. Computers & Fluids 35, 898–909.

Qian, Y. H., d'Humiéres, D., Lallemand, P., 1992. Lattice BGK models for Navier-Stokes equation. Europhysics Letters 17(6), 479–484.

Seta, T., Hayashi, K., Tomiyama, A., 2018. Analytical and numerical studies of the boundary slip in the immersed boundary-thermal lattice Boltzmann method. International Journal of Numerical Methods in Fluids 86(7), 454–490.

Seta, T., Rojas, R., Hayashi, K., Tomiyama, A., 2014. Implicit-correction-based immersed boundary–lattice Boltzmann method with two relaxation times. Physical Review E 89, 023307.

Sethian, J., 2001. Evolution, implementation, and application of level set and fast marching methods for advancing fronts. Journal of Computational Physics 169, 503–555.

Sussman, M., Smereka, P., Osher, S., 1994. A level set approach for computing solutins to incompressible two-phase flow. Journal of Computational Physics 114, 146–159.

Torii, R., Oshima, M., Kobayashi, T., Takagi, K., Tezduyar, T. E., 2006. Computer modeling of cardiovascular fluid-structure interactions with the deforming-spatial-domain/stabilized space-time formulation. Computer Methods in Applied Mechanics and Engineering 195(13-16), 1885–1895.

Weichert, F., Mertens, C., Walczak, L., Kern-Isberner, G., Wagner, M., 2013. A novel approach for connecting temporal-ontologies with blood flow simulations. Journal of Biomedical Informatics 46, 470–479.

Yamaguchi, T., 2008. Multi-scale computational biomechanics of arterial diseases. Annals of nanoBME 1, 5–14.

List of Tables

Table A.1: Numbers of computational cells, (N_x, N_y, N_z), in each direction

Case	Resolution 1	Resolution 2
1	$(64, 63, 74)$	$(128, 125, 148)$
2	$(64, 66, 48)$	$(128, 131, 96)$
3	$(64, 62, 58)$	$(128, 123, 114)$
4	$(64, 62, 56)$	$(128, 123, 112)$

Table A.2: Effects of Λ on numerical stability in TRT simulations (Case 3, Resolution 1. N: No, Y: Yes)

Λ	$1/4$	$3/16$	$1/6$	$1/12$	$1/100$	$1/200$	$1/400$	$1/10^4$
Stable	N	N	N	N	N	Y	Y	Y

Table A.3: Effects of Λ on numerical stability in TRT simulations (Case 4, Resolution 2. N: No, Y: Yes)

Λ	$1/4$	$3/16$	$1/6$	$1/12$	$1/20$	$1/40$	$1/100$	$1/200$
Stable	N	N	N	N	N	Y	Y	Y

Table A.4: Comparisons of $\widetilde{\tau}_W$ between Casson and Newtonian fluids. Changes in τ_W defined by $[\tau_W(Bi = 0) - \tau_W(Bi = 0.1)]/\tau_W(Bi = 0.1)$ are also given in the third rows in each case.

Case	Bi	Mean $\widetilde{\tau}_W$	$\max(\widetilde{\tau}_W)$	$\min(\widetilde{\tau}_W)$
1	0.1	0.121	0.33	0.0054
	0.0	0.110	0.29	0.0029
		-9.1%	-14%	-46%
2	0.1	0.175	0.42	0.029
	0.0	0.176	0.42	0.034
		0.5%	0.7%	15%
3	0.1	0.047	0.10	0.0082
	0.0	0.044	0.10	0.0050
		-6.0%	0%	-39%
4	0.1	0.024	0.077	0.0021
	0.0	0.021	0.066	0.00057
		-12%	-14%	-73%

List of Figures